nature communications

Article

https://doi.org/10.1038/s41467-026-72160-x

Uniform and ordered self-assembled hole-selective layers driven by π-π interactions for efficient perovskite-silicon tandem solar cells

Received: 14 December 2025

Accepted: 9 April 2026

Published online: 24 April 2026

Check for updates

Ming Luo[1,2,7], Zhou Liu[3,7], Qi Huang[1,7], Yifan Chen[1], Zhijie Wang[1,2], Dongrui Jiang[1,2], Rui Xia[3], Danni Yu[3], Rui He[3], Dongsheng Yan[2], Yi Mo[1,3], Xueling Zhang[3], Shengfan Wu[4], Fengxian Xie[1], Yingguo Yang[5], Wallace C. H. Choy[6], Yifeng Chen[3], Yang Wang[2] ✉, Jifan Gao[3] ✉, Junhao Chu[1] & Hong Zhang[1] ✉

Self-assembled molecules (SAMs) are promising hole-selective layers for high-performance perovskite tandem solar cells. However, their inhomogeneous distribution and disordered packing on substrates lead to interfacial energy losses, limiting further improvements in efficiency and stability. Here, we design a SAM, Me-Ph2*m*PACz, through *meta*-disubstitution of dimethylcarbazole moieties on a phenyl linker. Compared to its monosubstituted carbazole counterpart, Me-Ph*p*PACz, Me-Ph2*m*PACz exhibits stronger adsorption energy and suppresses intermolecular hydrogen bond interaction via π-π stacking interactions. This inhibits the formation of large micelles, promoting a uniform, ordered and thermoresistant hole-selective layer. The resulting multilayer configuration retards crystallization and alleviates residual stress in the perovskite film, thereby reducing non-radiative recombination at the buried interface and enhancing hole extraction. The implementation of Me-Ph2*m*PACz as the hole-selective layer in 1.68 eV perovskite solar cells reduces interfacial non-radiative losses from 168 mV to 124 mV, accompanied by an increase in power conversion efficiency from 21.82% to 23.14%. The corresponding perovskite-silicon tandem solar cells achieve a champion PCE of 33.40% (certified 32.45% at National Renewable Energy Laboratory, NREL). Furthermore, encapsulated tandem devices based on Me-Ph2*m*PACz demonstrate exceptional stability, retaining 83% of their initial efficiency after 1000 h of maximum power point tracking under one-sun illumination at 85 °C in air. This work opens an avenue for designing high-performance and durable self-assembled molecules for perovskite tandem photovoltaics.

Solution-processed inverted perovskite solar cells (PSCs) represents a cost-effective and scalable photovoltaic technology[1–3], and their compatibility with tandem architectures further enhances their commercial potential[4,5]. Certified efficiencies have reached 27.3% for single-junction and 34.85% for perovskite/silicon tandem cells[6]. This progress is closely linked to advances in hole-transport layers[7–10], particularly the emergence of self-assembled molecules (SAMs) as replacements for conventional hole-transporting materials such as

A full list of affiliations appears at the end of the paper. ✉e-mail: yangwang@fudan.edu.cn; jifan.gao@trinasolar.com; hzhangioe@fudan.edu.cn

PTAA and PEDOT:PSS in inverted PSCs[11,12]. Composed of an anchoring group, a linker, and a conjugated terminal unit, SAMs bind to metal oxides and enable efficient hole extraction with low optical and electrical losses. Furthermore, their molecular design allows fine-tuning of energy levels, extraction capability, and stability, making SAMs adaptable to various bandgaps and device configuration. However, a common limitation of SAMs lies in their inherent tendency toward aggregation, leading to non-uniform films, disordered packing, and poor charge transport properties. These issues increase interfacial non-radiative recombination and hinder further improvements in the efficiency and stability of both single-junction and tandem solar cells.

SAM aggregation originates from their intrinsic amphiphilic character[13,14], which drives micelle formation in common processing solvents rather than discrete molecules. To address this, several strategies focus on manipulating intermolecular interaction of SAM molecules during deposition or assembly. The co-solvent approach uses additives such as *N*,*N*-Dimethylformamide (DMF) or Dimethylsulfoxide (DMSO) to dissociate micelles, promoting denser SAM coverage[14,15]. By employing auxiliary molecules that disrupt aggregation through non-covalent interactions[16–19], molecular doping is another way to enhance film homogeneity and promotes favorable perovskite crystallization at the buried interface[20,21]. In co-SAM systems, a second SAM molecule is added to enhance packing[22] wettability,[23,24], and energy-level alignment while dispersing phosphonic acid clusters[25,26]. Alternatively, rational molecular design can intrinsically suppress aggregation—via steric hindrance or conformational distortion—while preserving efficient charge transport[27–30]. A key consideration in designing such molecular structures is the balance of π−π interactions. While excessive π−π stacking leads to detrimental aggregation, moderated interactions enable densely packed, ordered multilayers that support efficient hole transportation[31–33]. Thus, advancing SAM-based interfaces requires ingenious molecular design strategies that simultaneously inhibit aggregation and promote vertical charge conduction.

Herein, we synthesized a SAM, Me-Ph2*m*PACz, featuring a benzene-ring linker symmetrically functionalized with dual carbazole units at the *meta*-positions. Dimer interaction analysis reveals that this *meta*-disubstitution strategy enhances the continuity of intermolecular π−π stacking while reducing hydrogen-bond interaction between anchoring groups, thereby suppressing the formation of undesired large-sized SAMs clusters and yielding smaller molecular micelles. X-ray diffraction and grazing-incidence wide-angle X-ray scattering confirm that the strengthened π−π interactions promote a more uniform, well-ordered, and compact multilayer configuration on the substrate. This optimized interface results in more homogeneous potential distribution, improved energy-level alignment with the perovskite layer, and consequently more efficient hole extraction. Furthermore, it retarded crystallization and alleviates residual strain during perovskite crystallization, reducing non-radiative recombination at the buried interface. As a result, wide-bandgap (1.68 eV) PSCs incorporating Me-Ph2*m*PACz achieve an increase in efficiency from 21.82 to 23.14%. The perovskite−silicon tandem devices achieved a champion PCE of 33.40% (certified 32.45% at NREL), with an improved V_{OC} of 1.97 V, an FF of 83.1% and a J_{SC} of 20.40 mA cm^{-2}. Critically, the multilayer configuration of Me-Ph2*m*PACz on ITO/NiO_x exhibits robust thermal stability—with negligible variance after 1000 h of continuous aging at 85 °C—which translates into exceptional device performance: encapsulated tandem devices retain 83% of their initial efficiency after 1000 h of MPPT under one-sun illumination at 85 °C in air. Our work demonstrates a rational molecular design strategy that concurrently suppresses SAM aggregation and enhances hole extraction, offering a promising approach to high-performance interfaces for perovskite photovoltaics.

Results

Figure 1 illustrates the molecular design of the SAMs, along with characterization of their self-assembly behavior. As shown in Fig. 1a, reference molecule Me-Ph*p*PACz was previously reported for its good stability due to the rigid phenyl linker[34], and Me-Ph2*m*PACz was developed in this work. The latter was obtained by relocating the terminal 3,6-di-*tert*-butylcarbazolyl units to the two *meta*-positions relative to the phosphonic acid anchors. The synthetic routes are provided in Supplementary Fig. 1, and the structures of both molecules were confirmed by ^{1}H, ^{13}C, ^{31}P NMR spectroscopy and high-resolution mass spectrometry (Supplementary Figs. 2–17). Frontier orbital analysis (Supplementary Fig. 18) indicates more delocalized electron distribution in Me-Ph2*m*PACz, suggesting enhanced molecular stability[34–36]. Density-functional theory calculations reveal a higher adsorption energy of Me-Ph2*m*PACz on NiO_x (3.41 eV) compared to Me-Ph*p*PACz (2.46 eV), consistent with its larger interfacial charge transfer (Fig. 1b). The *meta*-dual-substitution also confers a larger dipole moment (1.27 Debye for Me-Ph2*m*PACz vs. 1.18 Debye for Me-Ph*p*PACz) (Fig. 1c), which is expected to promote stronger anchoring and more effective energy-level modification on NiO_x.

To understand the self-assembly behavior, we analyzed intermolecular interactions within SAM dimers (Fig. 1d, e). In Me-Ph*p*PACz, the substantial torsion angle between the carbazole and the phenyl linker disrupts π−π orbital overlap, leading to discontinuous stacking near the linker-terminal group junction. In contrast, the more planar *meta*-substituted molecular geometry of Me-Ph2*m*PACz with two large carbazolyl rings enables extended, continuous π−π interactions throughout the entire dimer, as visualized by the broader and denser contours of electron density (red frame, Fig. 1d). This continuous π-electron system also weakens hydrogen-bonding between phosphonic acid anchors (Supplementary Fig. 19), reducing the bonding that typically hinders micelle disassembly during film formation. Additionally, Supplementary Fig. 20 indicates stronger charge transfer between Me-Ph2*m*PACz and the perovskite layer, irrespective of whether the SAM adsorbs in a parallel or perpendicular orientation on the perovskite surface. Dynamic light scattering (DLS) validates this trend: Me-Ph*p*PACz contains polydisperse aggregates spanning hundreds of nanometers, whereas Me-Ph2mPACz yields clusters below 10 nm, reflecting a lower energy barrier for achieving uniform thin films (Fig. 1f). The degree of order in self-assembled films was probed by X-ray diffraction (XRD) on ITO/NiO_x substrates (Fig. 1g). While Me-Ph*p*PACz films show no crystalline peaks, a distinct reflection at ~8° appears for Me-Ph2*m*PACz, indicating a more ordered packing of SAM molecules. To gain a deeper understanding of the packing modes of the two SAMs, we characterized them using GIWAXS (Fig. 1h). Compared to Me-Ph*p*PACz, the Me-Ph2*m*PACz sample exhibits weaker background signals (Supplementary Fig. 21), suggesting a higher molecular coverage. Both SAMs display strong signals along the q_z direction, indicating a predominantly out-of-plane orientation. However, Me-Ph*p*PACz shows multiple diffuse arcs in the out-of-plane direction at $q_z \approx 0.23$, 0.45, 0.5, 0.7, and 0.95 Å^{-1}, respectively, indicating its less ordered packing. In contrast, Me-Ph2*m*PACz exhibits a sharp diffraction spot at $q_z \approx 0.3$ Å^{-1}, signifying ordered out-of-plane π−π stacking. In the in-plane (IP) direction, both SAMs show weak π−π stacking signals, but for Me-Ph2*m*PACz, this signal shifts to a higher q value (≈ 0.32 Å^{-1}) and appears tilted with respect to the substrate. Considering that π−π packing is governed by the bulky carbazole groups, we attribute the weak IP π−π stacking signals to the layer that is directly anchored to the ITO or NiO_x substrate via chemical bonds (the anchoring layer), while the out-of-plane signals originate from the stacking layer on the top of the anchoring layer, with both layers coexisting[13,37]. This also explains why the IP signal of Me-Ph2*m*PACz is not perfectly parallel to the substrate: the *meta*-substitution of the carbazole groups in Me-Ph2*m*PACz induces a tilt in the π−π stacking

https://doi.org/10.1038/s41467-026-72160-x

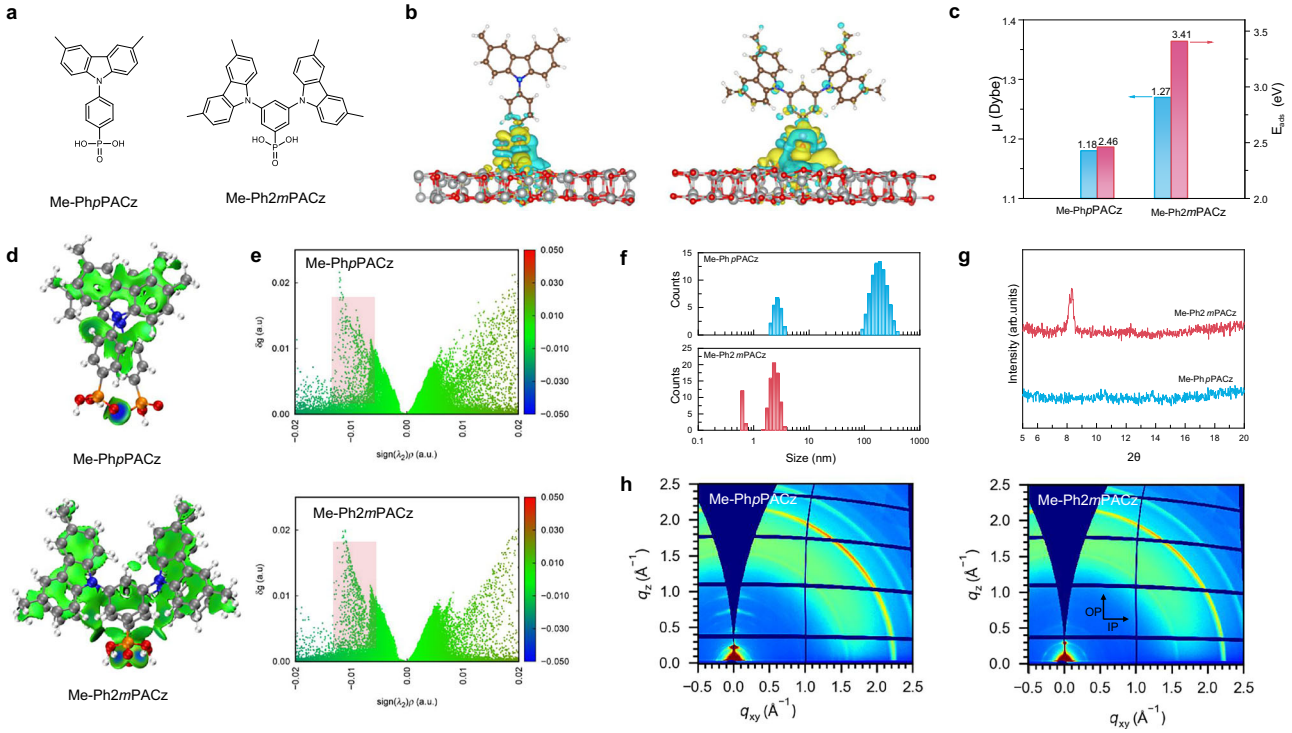

Fig. 1 | Molecular design. a Chemical structure of Me-Ph*p*PACz and Me-Ph2*m*PACz. **b** Schematic illustration of the charge density difference when Me-Ph*p*PACz (left) and Me-Ph2*m*PACz (right) contact NiO_x, respectively; Blue isosurface signifies electron depletion, while yellow represents electron accumulation. **c** Molecular dipole moment and adsorption energy of SAMs on NiO_x. **d** Schematic representation of the interaction force of Me-Ph*p*PACz (top) and Me-Ph2*m*PACz (bottom) dimers, analyzed and visualized by an independent gradient model based on Hirshfeld partition (IGMH). **e** IGMH analysis of π−π interactions in Me-Ph*p*PACz (top) and Me-Ph2*m*PACz (bottom) dimers. **f** Particle size distribution in solutions of Me-Ph*p*PACz and Me-Ph2*m*PACz as determined by DLS. **g** XRD of Me-Ph*p*PACz and Me-Ph2*m*PACz films deposited on ITO/NiOx substrates. **h** 2D GIWAXS image of Me-Ph*p*PACz (left) and Me-Ph2*m*PACz (right) deposited on ITO/NiOx substrates transferred to *q*-space.

direction of the anchoring layer. The upper stacking layer dominates the signal and is therefore expected to play a decisive role in determining the properties of the self-assembled film. From this perspective, the higher degree of order in Me-Ph2*m*PACz should be more favorable for the subsequent deposition of high-quality perovskite films and interface charge transfer, as will be discussed below.

We next correlated the properties of the self-assembled SAM films with their influence on the overlying perovskite layer. Cyclic voltammetry (CV) measurements determined the areal molecular density of Me-Ph2*m*PACz to be 3.06×10^{13} molecules cm^{-2}, which is 53% higher than that of Me-Ph*p*PACz (2.00×10^{13} molecules cm^{-2})[22,38] (Fig. 2a and Supplementary Fig. 22). The higher areal molecular density of Me-Ph2*m*PACz corresponds to better substrate coverage, owing to stronger SAM anchoring and easier micelle dissociation. Atomic force microscopy (AFM) was further used to measure the film morphology, and Me-Ph2*m*PACz showed a lower root-mean-square roughness (*Rq* =4.85 nm) than Me-Ph*p*PACz (*Rq*= 4.41 nm) when deposited on ITO/NiO_x substrate (Supplementary Fig. 23), indicating a more uniform surface. The enhanced uniformity was further corroborated electrically by Kelvin probe force microscopy (KPFM). The root-mean-square potential of Me-Ph2*m*PACz (42 mV) was markedly lower than that of Me-Ph*p*PACz (63 mV) (Fig. 2b), indicating a more homogeneous surface potential distribution[29]. The ITO/NiO_x/Me-Ph2*m*PACz surface also exhibited a reduced contact angle (88.9°) compared to ITO/NiO_x/Me-Ph*p*PACz (74.2°) (Supplementary Fig. 24), which is more favorable for subsequent perovskite deposition. Reduced contact angle and higher molecular density suggest that there might be more exposed phosphonic groups of ITO/NiO_x/Me-Ph2*m*PACz surface, which helps retard the crystallization process and passivate the buried defects. The ordered and densely packed SAMs are expected to improve charge transport properties. Indeed, conductance measurements based on hole-only devices (ITO/NiO_x/SAM/Ag) showed an increase in conductance values, from 0.167 S for Me-Ph*p*PACz to 0.211 S for Me-Ph2*m*PACz (Fig. 2c).

The well-ordered SAM morphology further translated into enhanced perovskite growth. AFM and scanning electron microscopy (SEM) indicated a smoother perovskite surface on Me-Ph2*m*PACz, with *Rq* decreasing from 10.9 to 8.64 nm (Supplementary Fig. 25). SEM further revealed fewer PbI_2 residues on the perovskite surface that is based on Me-Ph2*m*PACz (Supplementary Fig. 26a, b), a finding consistent with the weaker PbI_2 signal in XRD patterns (Supplementary Fig. 27a). Inspection of the buried interface showed that Me-Ph2*m*PACz facilitated cleaner detachment, often carrying adhered NiO_x nanoparticles due to its stronger anchoring—an evidence of its robust interfacial adhesion (Supplementary Fig. 26c, d). Cross-sectional SEM images further confirmed that perovskites grown on Me-Ph2*m*PACz exhibited smoother surfaces and fewer vertical grain boundaries (Fig. 2d). To quantify residual stress of the resulted perovskite film, surface grazing-incidence X-ray diffraction (GIXRD) was employed for $\sin^2\psi$ analysis (Supplementary Fig. 27b and 27c). The perovskite film on Me-Ph*p*PACz exhibited a compressive stress (slope = −0.17), whereas the film on Me-Ph2*m*PACz showed nearly stress-free characteristics (Fig. 2e). GIXRD of buried interface also showed improved crystallization (Supplementary Fig. 28) for perovskite grown on the Me-Ph2*m*PACz. To further elucidate the roles of SAMs in perovskite film formation, we performed in-situ PL spectroscopy to monitor crystallization dynamic during spin-coating and thermal annealing. During the spin coating process, the wet perovskite film on ITO/NiO_x/Me-Ph2*m*PACz exhibited a stronger photoluminescence (PL) signal[39,40], indicating a higher density of nuclei (Supplementary Fig. 29a, b), which

https://doi.org/10.1038/s41467-026-72160-x

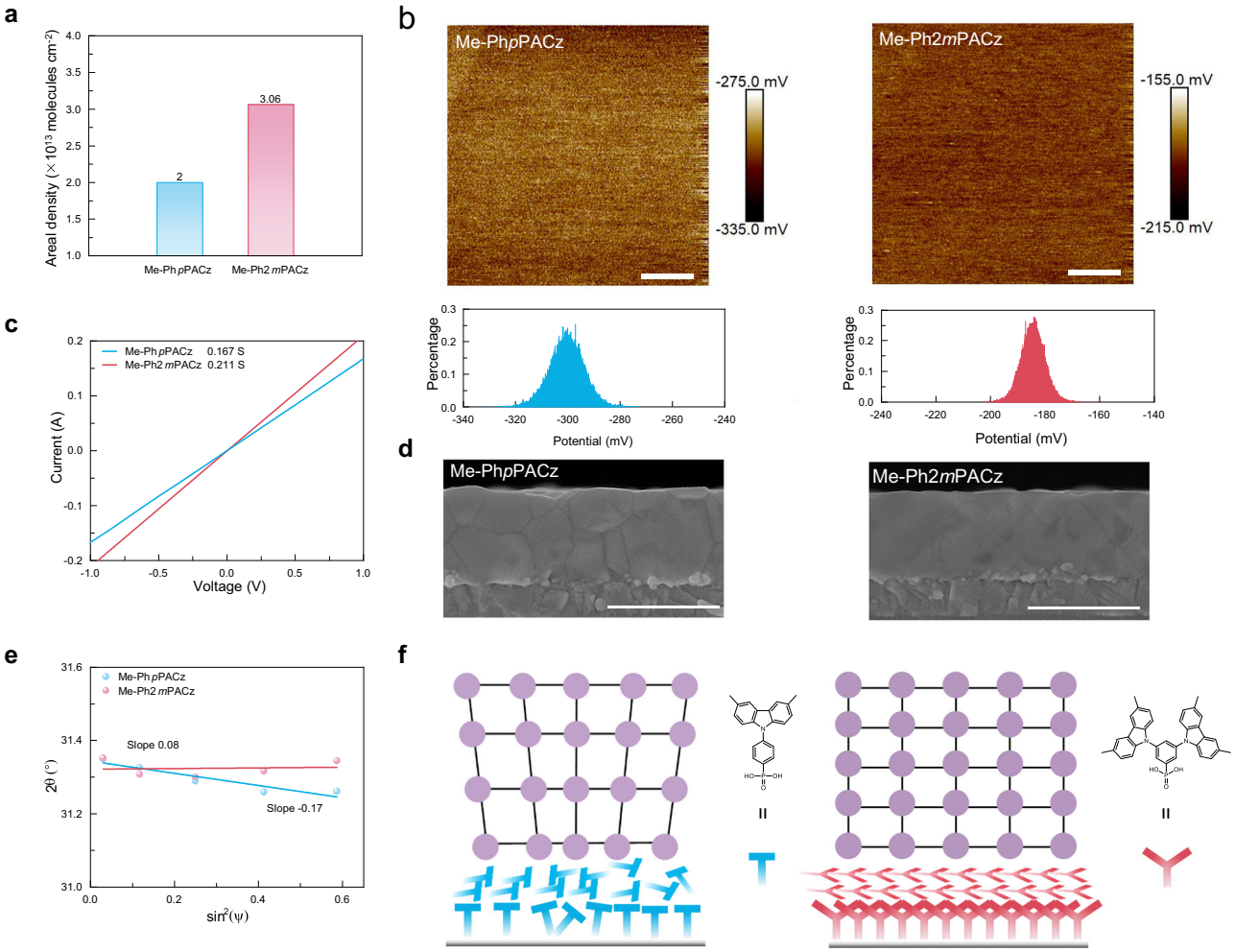

Fig. 2 | Properties of SAMs and influence on perovskite. a Areal density of SAMs on NiO_x/ITO substrate. **b** KPFM images and surface potential distribution of ITO/NiO_x/Me-Ph*p*PACz (left) and ITO/NiO_x/Me-Ph2*m*PACz (right). The scale bar is 2 µm. **c** Conductance of ITO/NiO_x/Me-Ph*p*PACz and ITO/NiO_x/Me-Ph2*m*PACz measured in N_2-saturated ACN solution under different voltage scan rates. **d** Cross-sectional SEM images of the perovskites on ITO/NiO_x/Me-Ph*p*PACz(left) and ITO/NiO_x/Me-Ph2*m*PACz (right) substrates. The scale bar is 500 nm. **e** Linear fit of 2θ-$\sin^2\psi$ of the perovskite films on ITO/NiO_x/Me-Ph*p*PACz and ITO/NiO_x/Me-Ph2*m*PACz substrates. **f** Schematic diagram of perovskite growth on the (left, with lattice stress) ITO/NiO_x/Me-Ph*p*PACz and (right, with mitigated lattice stress) ITO/NiO_x/Me-Ph2*m*PACz substrates.

may be ascribed to the enhanced wettability and more uniform SAM multilayer. During the annealing process, the initial PL quenching followed by enhancement of the PL signal is typically attributed to the dissolution and recrystallization of crystal grain during solvent evaporation (Fig. 29c, d)[39]. The decrease in PL intensity observed at the final stage of annealing corresponds to the formation of grain boundaries and the accumulation of thermal stress. For perovskite deposited on ITO/NiOx/Me-Ph2mPACz, the PL quenching and decreasing rate is much slower than that on ITO/NiOx/Me-PhpPACz, indicating a slower Ostwald ripening process[41]. Moreover, the continuously higher PL intensity during the final stage on ITO/NiOx/Me-Ph2mPACz suggests that the retarded recrystallization led to fewer defects and less stress[42]. The delayed recrystallization process might be caused by the coordination interaction between P = O group in Me-Ph2*m*PACz and perovskite component, as mentioned above. Integrating these observations with the earlier analysis regarding micelle in Fig. 1f, we propose the following mechanism, as depicted in Fig. 2f: The enhanced π−π interactions in Me-Ph2*m*PACz promote the formation of small-sized and uniform solution aggregates, which readily dissociate upon deposition to form a dense and ordered bilayer structure (~3.5 nm, Supplementary Fig. 23) that comprises an anchored layer adjacent to the substrate and a face-on π-π overlayer. This configuration accelerates perovskite nucleation while delaying the crystallization process, thereby releasing residual stress in the perovskite film during crystal growth. In contrast, Me-Ph*p*PACz forms larger aggregates with limited dissociation, yielding a less uniform multilayer that imparts residual stress to the overlying perovskite. The effective mitigation of such stress is crucial for reducing defect density and enhancing the long-term operational stability of PSCs.

We further monitored the durability of the two SAM molecules and the multilayer of Me-Ph2*m*PAC, since it is vital to the long-terme operation of the device. TGA analysis showed Me-Ph2*m*PACz (440 °C) exhibited a significantly higher 5% thermal decomposition temperature than Me-Ph*p*PACz (316 °C), indicating its better thermal stability (Supplementary Fig. 30). As shown in Supplementary Fig. 31, the crystallization signal of the Me-Ph2*m*PACz film remained almost unchanged after thermal aging, indicating that the film still retained its original uniform and ordered multilayer conformation. This finding was further confirmed by AFM test results. Supplementary Fig. 32 illustrates the changes in the overall morphology of the films before and after thermal aging. For the aged Me-Ph2*m*PACz, only negligible changes in roughness and morphology were observed. However, the roughness distribution of the Me-Ph*p*PACz film exhibited a significant deformation, with a noticeable increase in areas of higher roughness.

https://doi.org/10.1038/s41467-026-72160-x

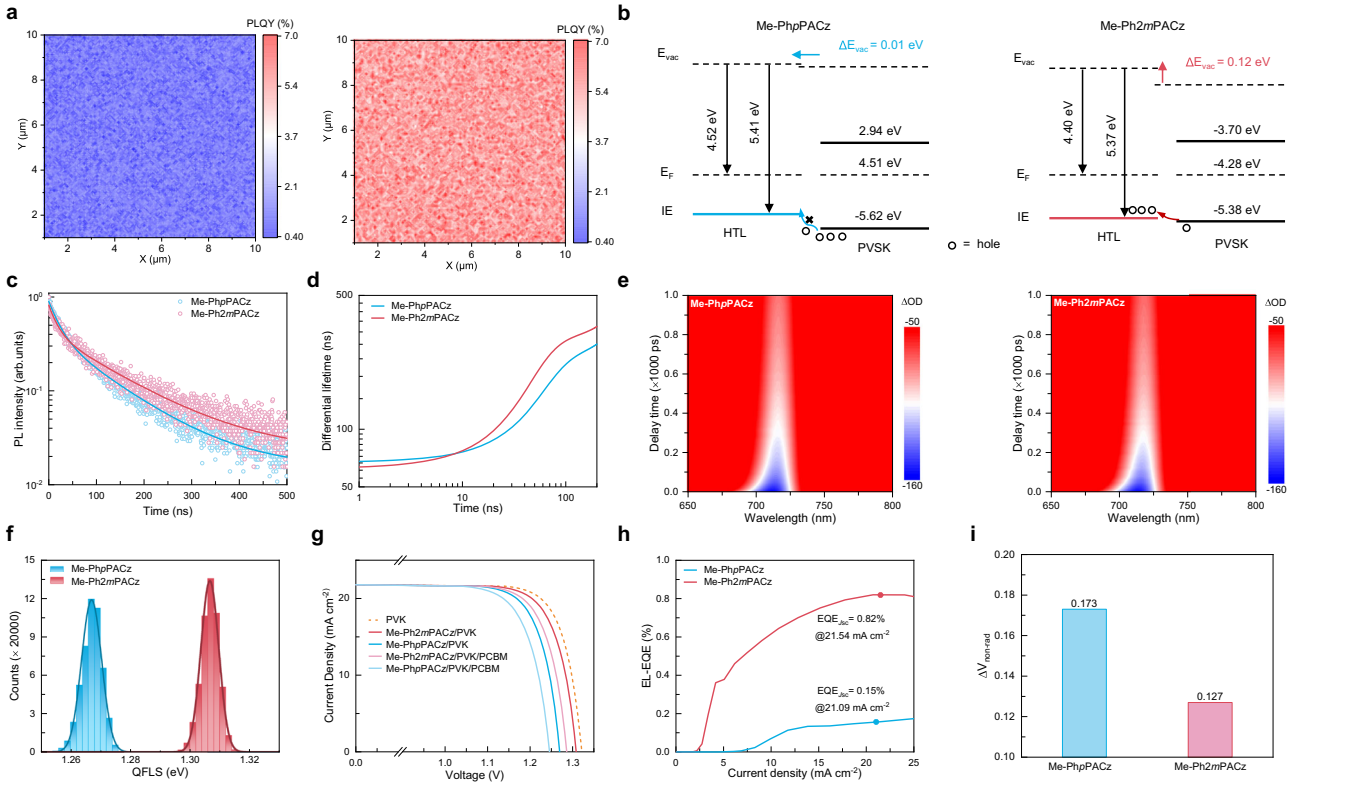

Fig. 3 | Carrier dynamics of perovskite. a PLQY mapping of perovskite films on ITO/NiO_x/Me-Ph*p*PACz and ITO/NiO_x/Me-Ph2*m*PACz. **b** energy-level diagrams of the perovskites and ITO/NiO_x/SAMs; **c** TRPL of perovskite film on ITO/NiO_x/Me-Ph*p*PACz and ITO/NiO_x/Me-Ph2*m*PACz. **d** Differential lifetime derived from TRPL measurements in (**c**). **e** Femtosecond transient absorption (fs-TA) test of perovskite film on ITO/NiO_x/Me-Ph*p*PACz and ITO/NiO_x/Me-Ph2*m*PACz. **f** QFLS calculated from (**a**). **g** *pseudo-JV* curves constructed from Me-Ph*p*PACz- and Me-Ph2*m*PACz-based stacks. **h** EQE_{EL} curves of the Me-Ph*p*PACz-and Me-Ph2*m*PACz-based devices. **i** Non-radiative voltage losses calculated from EQE_{JSC} in (**j**).

This was reflected in the morphological images by the emergence of numerous white spots of varying sizes, which should be attributed to the desorption and agglomeration of Me-Ph*p*PACz caused by long-term heating, due to its lower adsorption energy and weaker intermolecular interactions. Additionally, we rinsined the aged SAM films with DMF and compared the changes in SAM coverage by measuring the P/Sn elemental ratio before and after treatment using XPS (Supplementary Fig. 33 and Supplementary Table 1). As shown in Supplementary Table 1, the molecular retention of Me-Ph2*m*PACz self-assembled films after treatment was much higher than that of Me-Ph*p*PACz, demonstrating that Me-Ph2*m*PACz possesses stronger resistance to thermal and solvent rinsing compared to Me-Ph*p*PACz.

The dense, uniform, and ordered SAM structure is expected to facilitate efficient hole extraction. We therefore systematically investigated the carrier dynamics of perovskites deposited on Me-Ph*p*PACz and Me-Ph2*m*PACz. Ultraviolet–visible absorption (UV–vis) of the 1.68 eV perovskites revealed that Me-Ph2*m*PACz does not alter the bandgap but enhances the absorption (Supplementary Fig. 34a), which is likely due to improved film crystallinity (Fig. 27a). Steady-state PL showed a 3.4-fold increase in PL intensity on Me-Ph2*m*PACz (Supplementary Fig. 34b), indicating suppressed trap-assisted non-radiative recombination[43]. Results of large-area PL mapping ($50 \times 50\ \mu m^2$) further confirmed the stronger and more homogeneous PL emission from the Me-Ph2*m*PACz-based sample (Supplementary Fig. 35). Consistently, its PLQY was also much higher and more spatially uniform (Fig. 3a), pointing to the role of an ordered SAM in suppressing non-radiative recombination.

Ultraviolet photoelectron spectroscopy was used to determine the energy-level alignment (Supplementary Fig. 36). The Fermi levels of ITO/NiO_x/Me-Ph*p*PACz and ITO/NiO_x/Me-Ph2*m*PACz were measured at −4.52 and −4.40 eV, respectively (Fig. 3b), which is consistent with the contact-potential trend from KPFM (Supplementary Table 2). The ionization energies (IE) of the substrates were −5.41 and −5.37 eV, respectively, aligning with the calculated HOMO levels of the respective SAMs. A vacuum level shift of 0.01 eV was observed between the perovskite and the Me-Ph*p*PACz buried interface, which increased to 0.12 eV for the perovskite/Me-Ph2*m*PACz, respectively. The higher vacuum level shift in Me-Ph2*m*PACz/perovskite interface can be attributed to the out-of-plane dipole formed by its face-on, densely packed SAM structure[44]. The ionization energy (IE) of the Me-Ph2*m*PACz film (IE = 5.37 eV) was closely matched to that of the perovskite film (IE = 5.38 eV), which contributed to the reduction of the hole transfer barrier and suppression of non-radiative recombination at the interface[33].

Time-resolved PL (TRPL) decay curves were fitted with a biexponential function (Fig. 3c and Supplementary Table 3). The perovskite on Me-Ph2*m*PACz exhibited a shorter τ_1 (17.34 ns vs. 21.48 ns for Me-Ph*p*PACz), associated with faster interfacial charge extraction, and a longer τ_2 (133.14 ns vs. 117.04 ns), reflecting suppressed non-radiative recombination. The derived differential lifetimes of TRPL results are shown in Fig. 3d. The first interval in the differential lifetime profile of Me-Ph2*m*PACz is shorter than that of Me-Ph*p*PACz. This process is dominated by the charge transfer process, verifying the superior interfacial charge extraction of Me-Ph2*m*PACz[45]. These results confirm that the extended conjugation and enhanced π−π stacking in Me-Ph2*m*PACz promote hole extraction and reduce non-radiative recombination losses. Femtosecond transient absorption (fs-TA) spectroscopy further confirmed this conclusion: a faster decay of the ground-state bleaching signal at 700–720 nm was observed for Me-Ph2*m*PACz (Fig. 3e, Supplementary Fig. 37, and Supplementary

https://doi.org/10.1038/s41467-026-72160-x

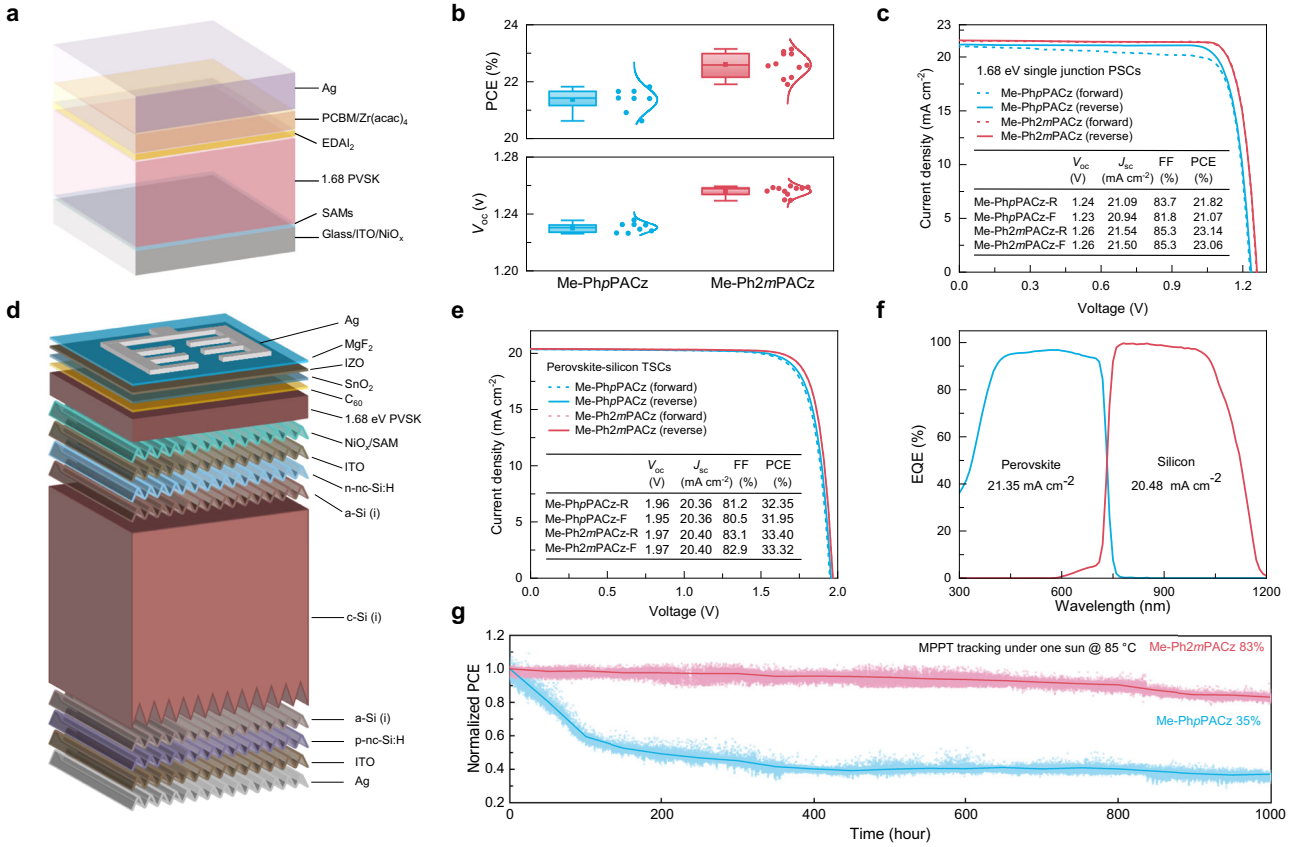

Fig. 4 | Photovoltaic performance and stability. a Schematic illustration of single junction 1.68 eV PSCs. **b** Statistics of PCE and V_{OC} of single junction 1.68 eV PSCs. **c** *J*–*V* characteristics of the champion single junction 1.68 eV PSCs. The box plots show the median (central line), 25th to 75th percentiles (box bounds), minima to maxima (whiskers), and individual data points (filled dots). **d** Schematic illustration of two-terminal (2T) perovskite/c-Si TSC. **e** *J*–*V* characteristics of the champion TSCs. **f** EQE curves of the Me-Ph2*m*PACz-based TSC. **g** MPPT of encapsulated TSCs under one-sun LED illumination at 85 °C in the air.

Table 4), indicating accelerated hole transfer[46]. Quasi-Fermi-level splitting (QFLS) was derived from the PLQY distributions (Fig. 3f). The Me-Ph2*m*PACz/perovskite sample showed narrower distributed QFLS with higher values (median = 1.318 eV), compared with the broader distribution of QFLS with lower QFLS values for Me-Ph*p*PACz (median = 1.264 eV). The improvement is attributed to the uniform SAM coverage, ordered molecular orientation, and reduced perovskite lattice strain.

To evaluate the implied photovoltaic performance, intensity-dependent steady-state PL was used to construct *pseudo-J-V* curves (Fig. 3g). Although interfacial recombination lowers the simulated efficiency relative to the optical limit, the Me-Ph2*m*PACz stack consistently outperformed the Me-Ph*p*PACz stack, achieving a *pseudo*-PCE of 24.58% with an implied V_{OC} of 1.307 V and a *pseudo*-FF of 86.12% (Supplementary Table5). Finally, electroluminescence external quantum efficiency (EQE_{EL}) measurements were performed to quantify non-radiative voltage losses in full devices (Fig. 3h). The Me-Ph2*m*PACz-based device exhibited a significantly higher EQE_{EL} (0.82% at J_{SC}) than the Me-Ph*p*PACz-based device (0.15%). Correspondingly, the non-radiative V_{OC} loss was reduced from 168 mV for Me-Ph*p*PACz to 124 mV for Me-Ph2*m*PACz (Fig. 3i), quantitatively confirming the superior interfacial passivation and charge extraction capability of the designed SAM.

To explore the impact of the SAMs on device performance, we fabricated 1.68 eV wide-bandgap perovskite solar cells (WBG PSCs, active area: 0.0804 cm^2) with the architecture of Glass/ITO/NiO_x/SAM/Perovskite/$EDAI_2$/PCBM/$Zr(acac)_4$/Ag (Fig. 4a). Statistical analysis of the key photovoltaic parameters (Fig. 4b and Supplementary Fig. 38) confirms that Me-Ph2*m*PACz-based devices consistently outperform their Me-Ph*p*PACz counterparts, regardless of whether the perovskite layer is deposited by gas quenching or the anti-solvent method (Supplementary Fig. 41), indicating the versatility of the SAM multilayer. The champion Me-Ph2*m*PACz-based device achieves a PCE of 23.14% at reverse scan with a V_{oc} of 1.26, a J_{sc} of 21.54 mA cm^{-2}, an FF of 85.3%, and negligible hysteresis, a clear improvement over the Me-Ph*p*PACz -based champion device (a PCE of 21.82%, a V_{oc} of 1.24 V, a J_{sc} of 21.09 mA cm^{-2}, an FF of 83.7%, and significant hysteresis) (Fig. 4c). The gains in V_{oc} and FF stem from the enhanced hole extraction and suppressed non-radiative recombination enabled by the ordered SAM structure. This is further supported by a lower ideality factor (1.49 vs. 1.74 for Me-Ph*p*PACz, Supplementary Fig. 39a) and reduced dark current density (Supplementary Fig. 39b) in Me-Ph2*m*PACz devices, indicating diminished Shockley-Read-Hall recombination. Additionally, we measured the impedance spectrum (Supplementary Fig. 40). The R_{rec} obtained from equivalent circuit fitting of the PSC based on Me-Ph2mPACz is significantly higher than that of the device based on Me-PhpPACz, indicating that non-radiative recombination in the device is effectively reduced. The improved J_{sc} is consistent with the higher conductance of the Me-Ph2*m*PACz film and is corroborated by external quantum efficiency measurements, which show a slightly higher integrated current (20.51 vs. 20.46 mA cm^{-2}) without a shift in bandgap (Supplementary Fig. 39c and 39d).

We subsequently integrated the SAM-based perovskite top cell with a silicon heterojunction bottom cell to fabricate monolithic tandem devices (active area: 1.05 cm^2; structure and cross-sectional SEM in Fig. 4d and Supplementary Fig. 42, respectively). The box plots of the nine independent devices based on different SAMs provides a direct comparison (Supplementary Fig. 43). The photovoltaic values

averaged over nine tandem devices indicate a PCE of 33.12%, a V_{OC} of 1.97 V, an FF of 82.7% and a J_{SC} of 20.35 mA cm^{-2} with Me-Ph2*m*PACz, compared with a PCE of 31.76%, a V_{OC} of 1.96 V, an FF of 79.9% and a J_{SC} of 20.29 mA cm^{-2} with Me-Ph*p*PACz (Fig. 4e). To more intuitively demonstrate the superiority of the SAM molecular design in this work, we also fabricated tandem devices using 2PACz (commonly used as a control) as the HTL for a direct comparison under the same conditions[10]. However, the 2PACz-based champion device only showed an inferior PCE of 30.84% at reverse scan (30.38% at forward scan) with stabilized efficiency of 30.40%, due to a fairly low V_{OC} of 1.90 V and an FF of 79.9% (Supplementary Fig. 43e) (comparable to reported values). With an improved V_{OC} 1.97 V and an FF of 83.1%, the tandem device based on Me-Ph2*m*PACz achieves a champion PCE of 33.40% at reverse scan (33.32% at forward scan) with stabilized efficiency of 33.17%, compared with a reverse scan value of 32.35% (31.95% at forward scan) with stabilized 32.11% for the tandem with Me-Ph*p*PACz. This tandem configuration has been sent to independently certified as 32.45% by the National Renewable Energy Laboratory (NREL) (Supplementary Fig. 44). The observed significant improvements in V_{oc} and FF are probably attributable to the high-performance of single-junction PSCs, which can be linked to the accelerated hole extraction and effective suppression of non-radiative recombination at the optimized SAM/perovskite interface. The photogenerated J_{SC} values of 21.35 and 20.48 mA cm^{-2} were obtained for the perovskite and silicon subcells in tandem device with Me-Ph2*m*PACz, respectively (Fig. 4f).

The robust and ordered SAM layer also enhanced operational stability. Unencapsulated single-junction WBG PSCs based on Me-Ph2*m*PACz retained 95% of their initial efficiency after 1000 h of maximum power point tracking (MPPT) under 1-sun LED illumination at 25 °C in N_2, whereas Me-Ph*p*PACz-based device degraded to 88% of their initial PCE (Supplementary Fig. 45). For encapsulated perovskite-silicon tandem solar cells (TSCs) (seen in Supplementary Fig. 46), the device based on Me-Ph2*m*PACz retained 83% of the initial efficiency after 1000 h of MPPT under 1-sun illumination at 85 °C in the air, outperforming their Me-Ph*p*PACz-based counterparts (only 35% of retainment) (Fig. 4g).

Discussion

In this work, we report a SAM, Me-Ph2*m*PACz, engineered through *meta*-dual-dimethyl-carbazole substitution. This molecular design employs enhanced π−π interactions to mitigate SAM aggregation, yielding a dense, well-ordered, and thermally robust multilayer on the substrate. The resulting SAM/perovskite interface effectively mitigates residual strain, homogenizes the surface potential, and optimizes energy-level alignment, thereby facilitating efficient hole extraction and significantly reducing non-radiative recombination. As a result, 1.68 eV single-junction PSCs deliver a PCE of 23.14%, and perovskite-silicon tandem cells attain a PCE of 33.40% (certified at 32.45% by NREL). And the encapsulated tandem devices retain 83% of the initial PCE after 1000 h under continuous 1-sun LED illumination at 85 °C in the air. This study establishes a paradigm for designing high-performance and durable SAMs for perovskite tandem photovoltaics.

Methods

Materials

Conductive Indium tin oxide (ITO) substrates (15 Ω sq^{-1}) with 20 × 20 mm dimension were purchased from Hua Nan Xiang Cheng Technology Co., Ltd. NiO_x nanoparticles (NPs) were synthesized according to previous work[47]. Self-assembled monolayer (SAM) of Me-Ph*p*PACz and Me-Ph2*m*PACz were synthesized according to synthetic route depicted in Supplementary Fig. 1. Aluminum oxide (Al_2O_3) NPs dispersing in isopropanol (IPA), DMF, and DMSO were purchased from Sigma-Aldrich. Dimethylammonium iodide (DMAI), cesium iodide (CsI), formamidinium iodide (FAI), and Ethanediamine dihydroiodide ($EDAI_2$) were purchased from Greatcell Solar. Lead bromide ($PbBr_2$) and lead chloride ($PbCl_2$) were purchased from Advanced Election Technology Co., Ltd. Lead iodide (PbI_2) was purchased from Alfa Aesar.[6,6]-phenyl-C61-butyric acid methyl ester (PCBM) was purchased from Nano-C. Zirconium (IV) acetylacetonate ($Zr(acac)_4$) purchased from Shanghai Aladdin Biochemical Technology Co., Ltd.

Chemical reagents and solvents used for SAM molecules synthesis: 1-bromo-4-iodobenzene, 1-bromo-3,5-difluorobenzene, triethylamine, bromotrimethylsilane (TMSBr), extra-dry DMF, 1,4-dioxane, dichloromethane, methanol, and deuterium reagents were purchased from J&K Scientific. 3,6-imethyl-9H-carbazole, Cesium carbonate (Cs_2CO_3), potassium acetate, palladium(II) acetate, 1,1-bis(diphenylphosphino)ferrocene (dppf), and diethyl phosphite were purchased from Energy Chemical Co. Ltd. Anhydrous sodium sulfate (Na_2SO_4) and toluene was purchased from Sinopharm Chemical Reagent Co., Ltd. Copper(I) iodide and cyclohexane-1,2-diamine (DMACH) was purchased from Shanghai Aladdin Biochemical Technology Co., Ltd. Potassium phosphate (K_3PO_4) was purchased from Shanghai Macklin Biochemical Co., Ltd.

Fabrication of single-junction WBG PSCs

The pre-patterned ITO substrates were cleaned and treated with UV−ozone for 20 min. The 10 mg mL^{-1} NiO_x NPs in deionized water and IPA (3:1) were spun onto ITO substrates at 3000 r.p.m. for 30 s and annealed at 100 °C for 10 min under ambient conditions. Then, the obtained NiO_x films were immediately transferred into a nitrogen-filled glovebox. A 0.5 mg/mL solution of Me-Ph*p*PACz or Me-Ph2*m*PACz (EtOH:DMF = 3:1) was spun-coated statically at 5000 rpm for 30 s onto ITO substrates and annealed at 150 °C for 10 min. The perovskite absorber layers were deposited in the N_2-filled glove box with controlled H_2O and O_2 levels <0.1 ppm, and the temperature was monitored to be 22–24 °C. The perovskite precursor with a composition of $Cs_{0.3}FA_{0.6}DMA_{0.1}Pb(I_{0.87}Br_{0.13})_3$ (1 M) was prepared by dissolving stoichiometric amounts of PbI_2, $PbBr_2$, $PbCl_2$, CsI, FAI, and DMAI in a mixed solvent of DMF and DMSO (4:1, v/v), with an additional 2 mol% $PbCl_2$ added to promote crystallization. Fifty microliters of the precursor solution was drop-cast onto the hole-transport layer (HTL) substrate. The substrate was spun at 2000 r.p.m. for 15 s with an acceleration of 1000 r.p.m. s^{-1} at first, and then at 4000 r.p.m. for the 45 s with an acceleration of 2000 r.p.m. s^{-1}, the nitrogen gun was vertically positioned 5 cm above the top of the substrates and the gas flow started after 30 s of the spin and duration of 20 s when the gas flow pressure was 0.3 MPa. Then, the perovskite wet-films were annealed at 100 °C for 20 min after aging 50 s. For the anti-solvent method, the perovskite precursor concentration was increased to 1.15 M, and 200 µL of anisole was dropped onto the film 10 s before the completion of spinning. The resulting perovskite film was immediately annealed at 100 °C for 20 min without the aging step. 1 mg mL^{-1} Ethanediamine dihydroiodide (EDAI) was spun-coated dynamically at 5000 rpm for 30 s onto perovskite layer and annealed at 100 °C for 5 min. The 23 mg mL^{-1} of $PC_{61}BM$ solution in chlorobenzene (CB) was spin-coated at 2500 r.p.m. for 40 s and then annealed at 70 °C for 10 min. 2 mg mL^{-1} of $Zr(acac)_4$ solution in IPA was spin-coated at 4000 r.p.m. for 40 s and without annealing. 100 nm of Ag were thermally evaporated onto the perovskite film at deposition rates of 0.1 Å s^{-1}–1 Å s^{-1}, respectively.

Fabrication of perovskite-silicon TSCs

The silicon bottom cells were fabricated using n-type Czochralski (CZ) silicon wafers with a resistivity of 1–5 Ω·cm^{-1} and a thickness of approximately 250–300 µm. Initially, a double-sided symmetrical texturing process was then performed using a potassium hydroxide (KOH) solution, resulting in random pyramids with a height of 500–1000 nm on both surfaces. Subsequently, the wafers underwent a standard RCA cleaning procedure and then loaded into a plasma-

enhanced chemical vapor deposition cluster for the passivation and doped layers. Hydrogenated intrinsic amorphous silicon (i-a-Si:H) layers, each with a thickness of about 10 nm, were deposited on both the front and rear surfaces. This was followed by the deposition of a 20-nm-thick n-type hydrogenated nanocrystalline silicon (n-nc-Si:H) layer and a 30-nm-thick p-nc-Si:H layer on the front and rear side of the wafer, respectively. Subsequently, a 150-nm-thick indium tin oxide (ITO) layer was sputtered onto the rear side through a shadow mask defining an active area of $1.2 \times 1.2\ cm^2$. Silver (Ag) rear electrodes were then screen-printed onto the ITO layer, also through the same mask pattern. Finally, a 10-nm-thick ITO layer, serving as the tunnel recombination layer, was deposited on the front side. The completed silicon bottom cells were laser-cut into $2.5 \times 2.5\ cm^2$ substrates for subsequent tandem cell fabrication.

The silicon bottom cells were treated with UV–ozone for 20 min. A NiO_x NPs aqueous dispersion ($10\ mg\ mL^{-1}$) was deposited on the substrates by spin coating at 3000 rpm for 30 s with an acceleration of 1000 rpm/s, followed by thermal annealing at 100 °C for 10 min. The substrates were then immediately transferred into a nitrogen-filled glovebox. Next, $1\ mg\ mL^{-1}$ SAMs solution in EtOH: DMF (v/v 3:1) was spin-coated at 3000 rpm for 30 s with an acceleration of 1000 rpm/s, and annealed at 150 °C for 10 min. Then, 100 µl of the perovskite precursor solution (1.7 M) was spin-coated onto the substrates at 600 rpm for 6 s with an acceleration of 200 rpm/s, followed by 2000 rpm for 50 s with an acceleration of 2000 rpm/s, and 6000 rpm for 15 s with acceleration of 2000 rpm/s. During the spin-coating process, 300 µl of anisole was dropped onto the film at the 59–60th s. The resulting perovskite film was immediately annealed at 100 °C for 20 min. Subsequently, a $1\ mg\ ml^{-1}$ of $EDAI_2$ solution in isopropanol was spin-coated onto the perovskite films at 5000 rpm for 30 s, followed by annealing at 100 °C for 5 min. The completed substrates were transferred into a thermal evaporation chamber, where 9 nm of C_{60} was deposited at a rate of $0.05\ Å\ s^{-1}$ ~ $0.1\ Å\ s^{-1}$. Subsequently, 21 nm SnO_x was grown in an ALD chamber at 80 °C. Finally, 400 nm of Ag and 90 nm MgF_x was deposited in a thermal evaporation chamber. The final devices with a structure of nin-bottom wafer/NiO_x/SAM/Perovskite/C_{60}/SnO_2/Ag/MgF_x had an active area of $1.21\ cm^2$, with a masked aperture area of $1.05\ cm^2$ for photovoltaic measurements.

Molecular property simulation

The theoretical calculations were performed using the Gaussian 16 suite of programs[48]. The structures of different SAMS were optimized at the B3LYP-D3/def2-TZVP level of theory[49–53]. The negative electrostatic potential (ESP) region (red color) implies the electrophilic property, while the positive ESP (blue color) represent the nucleophilic one. The noncovalent interactions were performed via Multiwfn 3.8 programs[54,55].

Geometry model optimization and charge density difference/interaction

The independent gradient model based on Hirshield partition[56] was conducted for SAMS top to investigate the weak interaction within SAMS. And the color-filled gradient isosurface maps intuitively exhibit the interaction area and corresponding strength. The differential charge density of SAMS top and bottom interface were carried out using the Vienna Ab initio Simulation Package[57] with the projector augmented wave method[58]. The exchange functional was treated using the Perdew–Burke–Emzerhof functional[59]. The energy cutoff for the plane wave basis expansion was tuned to be 400 eV. Partial occupancies of the Kohn–Sham orbitals were permitted by the Gaussian smearing method and a width of 0.2 eV. The Brillouin zone was sampled with Monkhorst mesh of $2 \times 2 \times 1$ for the optimization for all the structures. The self-consistent calculations apply a convergence energy threshold of 10^{-5} eV, and the force convergency was tuned to be $0.05\ eV\ Å^{-1}$.

Reporting summary

Further information on research design is available in the Nature Portfolio Reporting Summary linked to this article.

Data availability

All the data supporting the findings of this study are available within this article and its Supplementary Information. Any additional information can be obtained from corresponding authors upon request. Source data are provided with this paper.

References

1. Green, M. A. et al. The emergence of perovskite solar cells. *Nat. Photonics* **8**, 506–514 (2014).
2. Burschka, J. et al. Sequential deposition as a route to high-performance perovskite-sensitized solar cells. *Nature* **499**, 316–319 (2013).
3. Chen, C. et al. Perovskite solar cells based on screen-printed thin films. *Nature* **612**, 266–271 (2022).
4. Ramadan, A. J. et al. Methylammonium-free wide-bandgap metal halide perovskites for tandem photovoltaics. *Nat. Rev. Mater.* **8**, 822–838 (2023).
5. Yang, G. et al. Towards efficient, scalable and stable perovskite/silicon tandem solar cells. *Nat. Photonics* **19**, 913–924 (2025).
6. Green, M. A. et al. Solar cell efficiency tables (version 66). *Prog. Photovoltaics: Res. Appl.* **33**, 795–810 (2025).
7. Peng, W. et al. Reducing nonradiative recombination in perovskite solar cells with a porous insulator contact. *Science* **379**, 683–690 (2023).
8. Jiang, Q. & Zhu, K. Rapid advances enabling high-performance inverted perovskite solar cells. *Nat. Rev. Mater.* **9**, 399–419 (2024).
9. Zhang, B. et al. A cross-linked molecular contact for stable operation of perovskite/silicon tandem solar cells. *Science* **390**, 837–842 (2025).
10. Zhang, D. et al. Perovskite crystallization control via an engineered self-assembled monolayer in perovskite–silicon tandem solar cells. *Nat. Photonics* **20**, 40–48 (2025).
11. Al-Ashouri, A. et al. Monolithic perovskite/silicon tandem solar cell with >29% efficiency by enhanced hole extraction. *Science* **370**, 1300–1309 (2020).
12. Levine, I. et al. Charge transfer rates and electron trapping at buried interfaces of perovskite solar cells. *Joule* **5**, 2915–2933 (2021).
13. Wu, M. et al. Reconstruction of the indium tin oxide surface enhances the adsorption of high-density self-assembled monolayer for perovskite/silicon tandem solar cells. *Adv. Funct. Mater.* **33**, 2304708 (2023).
14. Liu, M. et al. Compact hole-selective self-assembled monolayers enabled by disassembling micelles in solution for efficient perovskite solar cells. *Adv. Mater.* **35**, e2304415 (2023).
15. Peng, C. et al. Reinforcement of carbazole-based self-assembled monolayers in inverted perovskite solar cells. *ACS Appl. Mater. Interfaces* **17**, 10745–10754 (2025).
16. Liang, Y. et al. A matrix-confined molecular layer for perovskite photovoltaic modules. *Nature* **648**, 91–96 (2025).
17. Zhang, Z. et al. Monodisperse regulation of self-assembled monolayer via dipole molecules for efficient perovskite solar cells. *Angew. Chem. Int. Ed.* **64**, e202512660 (2025).
18. Qu, S. et al. Redox mediator-modified self-assembled monolayer stabilizes a buried interface in efficient inverted perovskite solar cells. *Energy Environ. Sci.* **18**, 3186–3195 (2025).
19. Zhao, H. et al. Synergistic self-assembled monolayers reinforce buried interface anchoring for high-efficiency tandem perovskite solar cells. *Angew. Chem. Int. Ed.* **64**, e202504237 (2025).
20. Pan, J. et al. Strong electron-withdrawing molecules facilitating pi-pi stacking and charge transfer complexes at buried interface and

enabling an inverted PSC with open-circuit voltage of 1.2 V. *Angew. Chem. Int. Ed.* **64**, e202514365 (2025).
21. Tao, R. et al. pH modulation for self-assembly-monolayer-type hole transport layer for efficient and stable perovskite-silicon double-junction solar cells. *Joule* **10**, 102314 (2026).
22. Park, S. M. et al. Low-loss contacts on textured substrates for inverted perovskite solar cells. *Nature* **624**, 289–294 (2023).
23. Su, Z. et al. Stereo-hindrance induced conformal self-assembled monolayer for high efficiency inverted perovskite solar cells. *Small* **20**, e2407387 (2024).
24. Shi, C. et al. Modulating competitive adsorption of hybrid self-assembled molecules for efficient wide-bandgap perovskite solar cells and tandems. *Nat. Commun.* **16**, 3029 (2025).
25. Peng, W. et al. A versatile energy-level-tunable hole-transport layer for multi-composition inverted perovskite solar cells. *Energy Environ. Sci.* **18**, 874–883 (2025).
26. Torres Merino, L. V. et al. Impact of the valence band energy alignment at the hole-collecting interface on the photostability of wide band-gap perovskite solar cells. *Joule* **8**, 2585–2606 (2024).
27. Zhou, J. et al. Molecular contacts with an orthogonal π-skeleton induce amorphization to enhance perovskite solar cell performance. *Nat. Chem.* **17**, 564–570 (2025).
28. Zhang, X. et al. A spiro-type self-assembled hole transporting monolayer for highly efficient and stable inverted perovskite solar cells and modules. *Energy Environ. Sci.* **18**, 468–477 (2025).
29. Wang, X. et al. Regulating phase homogeneity by self-assembled molecules for enhanced efficiency and stability of inverted perovskite solar cells. *Nat. Photonics* **18**, 1269–1275 (2024).
30. Gao, D. et al. High-efficiency perovskite solar cells enabled by suppressing intermolecular aggregation in hole-selective contacts. *Nat. Photonics* **19**, 1070–1077 (2025).
31. Yan, B. et al. Chiral Aza-helicene phosphonic acids for stabilizing efficient perovskite-silicon tandem solar cells. *Angew. Chem. Int. Ed.* **64**, e202509279 (2025).
32. Zhu, P. et al. Symmetry-driven engineering of long-range-ordered π–π stacking molecules for high-efficiency perovskite photovoltaics. *Nat. Synth.* **5**, 64–73 (2026).
33. Du, J. et al. Face-on oriented self-assembled molecules with enhanced π–π stacking for highly efficient inverted perovskite solar cells on rough FTO substrates. *Energy Environ. Sci.* **18**, 3196–3210 (2025).
34. Qu, G. et al. Conjugated linker-boosted self-assembled monolayer molecule for inverted perovskite solar cells. *Joule* **8**, 2123–2134 (2024).
35. Zhang, S. et al. Conjugated self-assembled monolayer as stable hole-selective contact for inverted perovskite solar cells. *ACS Mater. Lett.* **4**, 1976–1983 (2022).
36. Zhang, S. et al. Self-assembled π-conjugated hole-selective molecules for UV-resistant high-efficiency perovskite solar cells. *Angew. Chem. Int. Ed.* **64**, e202508782 (2025).
37. Qu, G. et al. Self-assembled materials with an ordered hydrophilic bilayer for high performance inverted Perovskite solar cells. *Nat. Commun.* **16**, 86 (2025).
38. Feng, Y. et al. Homogenized self-assembled molecules for inverted perovskite solar cells. *Angew. Chem. Int. Ed.* **64**, e202505876 (2025).
39. Li, S. et al. Solvent engineering enables tin-lead perovskite films with long carrier diffusion lengths and reduced tin segregation. *Nat. Commun.* **16**, 8072 (2025).
40. Pratap, S. et al. Out-of-equilibrium processes in crystallization of organic-inorganic perovskites during spin coating. *Nat. Commun.* **12**, 5624 (2021).
41. Cao, X. et al. Fabrication of perovskite films with large columnar grains via solvent-mediated Ostwald ripening for efficient inverted perovskite solar cells. *ACS Appl. Energy Mater.* **1**, 868–875 (2018).
42. Cai, W. et al. Interlayer reinforcement for improved mechanical reliability for wearable perovskite solar cells. *Energy Environ. Sci.* **17**, 8162–8173 (2024).
43. Al-Ashouri, A. et al. Conformal monolayer contacts with lossless interfaces for perovskite single junction and monolithic tandem solar cells. *Energy Environ. Sci.* **12**, 3356–3369 (2019).
44. Li, X. et al. Mapping the energy level alignment at donor/acceptor interfaces in non-fullerene organic solar cells. *Nat. Commun.* **13**, 2046 (2022).
45. Luo, Y. et al. Inductive effects in molecular contacts enable wide-bandgap perovskite cells for efficient perovskite/TOPCon tandems. *Nat. Commun.* **16**, 4516 (2025).
46. Liu, S. et al. Solvated-intermediate-driven surface transformation of lead halide perovskites. *Nat. Energy* **11**, 109–120 (2025).
47. Zhang, H. et al. Pinhole-free and surface-nanostructured NiOx film by room-temperature solution process for high-performance flexible perovskite solar cells with good stability and reproducibility. *ACS Nano* **10**, 1503–1511 (2016).
48. Frisch, M. J. et al. *Gaussian 16 Rev. A.03* (Wallingford, CT, 2016).
49. Becke, A. D. Density-functional exchange-energy approximation with correct asymptotic behavior. *Phys. Rev. A* **38**, 3098–3100 (1988).
50. Lee, C. et al. Development of the Colle-Salvetti correlation-energy formula into a functional of the electron density. *Phys. Rev. B* **37**, 785–789 (1988).
51. Grimme, S. et al. A consistent and accurate ab initio parametrization of density functional dispersion correction (DFT-D) for the 94 elements H-Pu. *J. Chem. Phys.* **132**, 154104 (2010).
52. Grimme, S. et al. Effect of the damping function in dispersion corrected density functional theory. *J. Comput. Chem.* **32**, 1456–1465 (2011).
53. Becke, A. D. Density-functional thermochemistry. III. The role of exact exchange. *J. Chem. Phys.* **98**, 5648–5652 (1993).
54. Lu, T. & Chen, F. Multiwfn: a multifunctional wavefunction analyzer. *J. Comput. Chem.* **33**, 580–592 (2012).
55. Lu, T. A comprehensive electron wavefunction analysis toolbox for chemists, Multiwfn. *J. Chem. Phys.* **161**, 082503 (2024).
56. Lu, T. & Chen, Q. Independent gradient model based on Hirshfeld partition: a new method for visual study of interactions in chemical systems. *J. Comput. Chem.* **43**, 539–555 (2022).
57. Kresse, G. & Furthmüller, J. Efficiency of ab-initio total energy calculations for metals and semiconductors using a plane-wave basis set. *Comput. Mater. Sci.* **6**, 15–50 (1996).
58. Blöchl, P. E. Projector augmented-wave method. *Phys. Rev. B* **50**, 17953–17979 (1994).
59. Perdew, J. P. et al. Generalized gradient approximation made simple. *Phys. Rev. Lett.* **77**, 3865–3868 (1996).

Acknowledgements

This work was financially supported by the National Key R&D Program of China (grant number 2024YFE0216900), the National Natural Science Foundation of China (grant numbers 52302229, 62574053, 22375051 and 52561160144), Basic Research Program of Jiangsu (grant number BK20250343), Shanghai Science and Technology Commission Program (25DZ3002001), the State Key Laboratory of Photovoltaic Science and Technology of China (grant number. 202401030301) and the Fudan University Nano Information Science Innovation Support Center Project, Ministry of Education of China. We thank the staff of beamlines BL02U2, BL17B1, and BL18U1 at SSRF for providing the beam time and User Experiment Assist System of SSRF for their help, GIWAXS setup is also supported by National Natural Science Foundation of China (grant number 12175298). The authors thank Prof. Guangzheng Zuo and Dr. Yuqian Liu for technical support in EIS measurements; Dr. Donghao Miao, Dr. Qianqian Wang, and Mr. Liucheng Gao for assistance with in-situ PL measurements; Dr. Hong Liu for SEM technical support; and Dr. Xinxin Lian for WBG perovskite recipe optimization and moral support.

Author contributions

H.Z. convinced the idea and supervised the project. M.L. synthesized the SAMs, fabricated and characterized the single junction devices and performed the stability tests of device. Z.L. and Y.M. fabricated and characterized the tandem devices. Q. H. performed the DFT simulation. Y.C. (Yifan Chen), Z.W., and D.J were responsible for the morphology characterization and analysis of perovskite film. R.X., D.Y. (DanniYu), R.H., and Y.M. were responsible for the encapsulation of tandem devices. D.Y. (DongshenYan) provided assistance with synthesis, and Y.W. provided the synthesis laboratory and participated in relevant discussions on the design and synthesis of SAMs. Y.Y. performed GIWAXS measurements and analysis guidance. X.Z., S.W., and F.X. provided guidance for the analysis of perovskite and SAM thin films. M.L. wrote the first draft, W.C., Y.C. (Yifeng Chen), H.Z., J.G., Y.W., and J.C. revised the manuscript. All authors contributed mentioned on the manuscript.

Competing interests

The authors declare the following competing interests: Hong Zhang and Ming Luo filled a Chinese patent related to this work (CN202511027586.5). The other authors declare no competing financial interests. All authors declare no competing non-financial interests.

Additional information

Supplementary information The online version contains supplementary material available at https://doi.org/10.1038/s41467-026-72160-x.

Correspondence and requests for materials should be addressed to Yang Wang, Jifan Gao or Hong Zhang.

Peer review information *Nature Communications* thanks Jingjing Xue, Stefaan De Wolf, and the other, anonymous, reviewer(s) for their contribution to the peer review of this work. A peer review file is available.

[1]State Key Laboratory of Photovoltaic Science and Technology, Shanghai Frontiers Science Research Base of Intelligent Optoelectronics and Perception, Institute of Optoelectronics, College of Future Information Technology, Fudan University, Shanghai, China. [2]College of Smart Materials and Future Energy, State Key Laboratory of Molecular Engineering of Polymers, Fudan University, Shanghai, China. [3]State Key Laboratory of Photovoltaic Science and Technology, Trina Solar, Changzhou, China. [4]School of Interdisciplinary Studies, Lingnan University, Hong Kong, China. [5]School of Microelectronics, Fudan University, Shanghai, China. [6]Department of Electrical and Electronic Engineering, The University of Hong Kong, Hong Kong, China. [7]These authors contributed equally: Ming Luo, Zhou Liu, Qi Huang. ✉e-mail: yangwang@fudan.edu.cn; jifan.gao@trinasolar.com; hzhangioe@fudan.edu.cn